Nano Energy 48 (2018) 536–542

Contents lists available at ScienceDirect

Nano Energy

journal homepage: www.elsevier.com/locate/nanoen

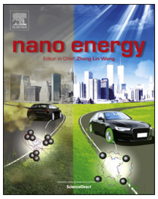

Full paper

Mixed cation perovskite solar cells by stack-sequence chemical vapor deposition with self-passivation and gradient absorption layer

Guoqing Tong[a,b], Huan Li[b], Guopeng Li[b], Ting Zhang[a], Chengdong Li[a], Linwei Yu[a,*], Jun Xu[a], Yang Jiang[b,*], Yi Shi[a], Kunji Chen[a]

[a] *National Laboratory of Solid State Microstructures and School of Electronics Science and Engineering/Collaborative Innovation Centre of Advanced Microstructures, Nanjing University, Nanjing 210093, PR China*
[b] *School of Materials Science and Engineering, Hefei University of Technology, Hefei 230009, PR China*

ARTICLE INFO

Keywords:
Perovskite solar cell
Cesium doping
Vapor deposition
Passivation
Gradient absorption layer

ABSTRACT

Mixed cation halide perovskite solar cells (PSCs), in a formula of ABX_3 where A is a mixture of formamidinium (FA) or cesium (Cs) cations, represent a promising new architecture to achieve largely improved stability and higher power conversion efficiency (PCE). While all these mixed-cation PSCs were synthesized via a solution method, we here propose and demonstrate a precisely tunable stack sequence physical-chemical vapor deposition (SS-PCVD) approach to prepare a mixed-cation absorber in CsBr-doped hybrid organic perovskite, which features a beneficial gradient bandgap profile to enable an improvement of PCE from 11.69% in pure $FAPbI_3$ to 18.22% in mixed-cation PSCs. Remarkably, an excellent stability in ambient exposure for 60 days has been achieved by a proper control of the CsBr cation incorporation and interface passivation. This new approach indicates a simple, precisely tunable and low cost fabrication strategy to implement high performance and scalable mixed-cation halide perovskite solar cells.

1. Introduction

Since the first report of hybrid perovskite solar cells (PSCs) with a power conversion efficiency (PCE) of 3.8%, recent years have witnessed a rapid progress in boosting the PCE of PSCs to a high PCE above 22% [1–6]. The perovskite material usually shares a common formula of ABX_3, where A stands for the cations of methylammonium (MA), formamidinium (FA) or cesium (Cs), while B for Pb or Sn and X for the halides of Cl, Br and I [7,8]. In order to boost the PCE, a variety of method has been explored to optimize the fabrication procedure, which includes the solution process, the vacuum deposition and the vapor-assisted solution process [9–12]. In all these methods, processing temperature control or post-growth annealing are found to be crucial, and thus mostly used, to improve the crystallinity and electric properties of the perovskite layer [13,14]. Further improvement of the PSCs, in pursuit of higher PCE and particularly of better stability against moisture exposure, demands also new wisdom in structural control and engineering, for example, by employing a novel material band gap profile or structure design in composite mixed-cation perovskite multilayers.

Formamidinium lead iodide ($HC(NH_2)_2PbI_3$, $FAPbI_3$) has been adopted as an alternative to $MAPbI_3$ in perovskite solar cells, because of a higher carrier mobility and a narrower bandgap of ~1.43 eV that enables a wider absorption spectrum to 860 nm [15–17]. A PCE of 16.01% (or 14.2%) has been achieved by employing the $FAPbI_3$ to replace $MAPbI_3$ as the absorption layer in a mesoscopic (or planar) PSC structure [16,18]. However, the preferable black photovoltaic phase of trigonal $FAPbI_3$ perovskite is only stable at a higher temperature above 160 °C, and is prone to decade into a yellow hexagonal non-perovskite phase at room temperature [19]. In parallel, pure inorganic perovskite materials of $CsPbX_3$ ($X = Cl, Br, I$) are also regarded as promising candidates for solar cells and very efficient luminescent high-energy radiation detectors [20–23]. However, compared to the $MAPbI_3$, the $CsPbI_3$ thin film materials suffers from a poor thermal stability at the room temperature, and thus difficult to implement in ambient condition [3]. In contrast, $CsPbBr_3$ exhibits an excellent stability even in a moisture condition. Recently, an all-inorganic perovskite solar cell, with $CsPbBr_3$ as the absorption layer in a multilayer structure of FTO/c-TiO_2/m-TiO_2/$CsPbBr_3$/carbon, has been reported with a high PCE of 6.7% and an excellent stability in air with a humidity of 95% for more than 3 months, and still without any performance degradation [20]. Unfortunately, the potential of $CsPbBr_3$ perovskite solar cell has been fundamentally limited by its wide bandgap of ~2.33 eV, which is inefficient to harvest the solar energy over the spectrum of standard AM

---

[*] Corresponding authors.
E-mail addresses: yulinwei@nju.edu.cn (L. Yu), apjiang@hfut.edu.cn (Y. Jiang).

https://doi.org/10.1016/j.nanoen.2018.04.012
Received 18 December 2017; Received in revised form 18 March 2018; Accepted 5 April 2018

1.5 illuminations.

In order to combine the high photocurrent in hybrid solar cells and the excellent stability of inorganic Cs-based PSCs, recent research efforts have been focused on controlling the composition and the stoichiometry of combined or mixed-cations perovskite materials [24–27]. Hyosung Choi et al. demonstrated Cs-doping in the perovskite ($MAPbI_3$) by adding CsI via typical solution process, and thus obtained a PCE of 7.68% in a perovskite solar cell of $Cs_xMA_{1-x}PbI_3$ [28]. Then, Jin-Wook Lee reported that the replacement of the $HC(NH_2)_2{}^+$ by Cs ion can help to improve both the optical properties and the stability in the moisture environment, with a notably high PCE of 16.5% obtained with 10% Cs-cation substitution [29]. What's more, Chenyi Yi and co-workers employed CsI, FAI, FABr and PbI_2 in a mixed solvent to realize a mixed-cation perovskite of $Cs_{.2}FA_{.8}PbI_{2.6}Br_{.4}$ and achieved a high PCE of 17.3% and excellent air stability for at least 1000 h without encapsulation [19]. Furthermore, Saliba and Park et al. introduced a new inorganic A-cation doping of Rb^+ (with an ionic diameter of 1.52 Å), which is slightly smaller than that of Cs^+ (of 1.67 Å), into the perovskite structure to accomplish a new kind of mixed-cation perovskite [30,31]. The performances of the PSCs with the A-cation in previous reports are summarized in the Table 1.

While the solution methods are widely adopted in the perovskite solar cell fabrication because of a simple, rapid and low cost processing, the fast reaction in the solution process, as well as the inhomogeneity and potential damage of mixed organic solvents to some extent, poses also a limitation to the tunability and optimization of the mixed-cation perovskite thin films [9,38]. In comparison, vapor deposition processes allowed a rather uniform deposition of high crystalline and high density perovskite materials, in a precisely tunable repeatable and scalable environment [9,39]. More importantly, large area perovskite thin films can be deposited with the standard industrial vacuum-vapor fabrication facilities. Apart from the organic-inorganic perovskite thin film via the vapor deposition method, the inorganic perovskite films, including $CsPbI_3$, $CsPbIBr_2$, $CsPbI_2Br$, were also produced via vacuum vapor deposition [11,33–35].

In this work, we proposed a new stack-sequence physical-chemical vapor deposition (SS-PCVD) and doping approach to accomplish a gradient inclusion and distribution of Cs cations into an overall perovskite thin film of $Cs_{.15}$ $FA_{.85}PbI_{2.85}Br_{.15}$ as an efficient light harvest layer. The non-uniform incorporation of Cs cations leads to a tailored gradient band gap profile that is favorable for both the carrier separation and establishing a distributed light absorption within the absorber layer. Compared to the pure $FAPbI_3$ and $MAPbI_3$, the gradient-band gap Cs_xFAPbI_3 thin film PSCs achieve a high photovoltaic performance with a PCE of 18.22%, a short current density J_{sc} of 22.82 mA cm^{-2}, an open-circuit voltage V_{oc} of 1.06 V with a fill factor of 75.1%. More importantly, the devices exhibited a high stability with PCE~10% after air-exposure for more than two months, indicating that the mixed perovskite by vapor deposition method provides a promising way to fabricate and engineer the PSCs, which has an important potential for achieving a scalable industrial implementation.

Table 1
A comparison of the performance of the mixed-cations perovskite solar cells reported in the literature and in this work.

Device	Method	V_{oc} (V)	J_{sc} (mA cm^{-2})	FF (%)	PCE (%)	Ref
$Cs_{.15}FA_{.85}PbI_{2.85}Br_{.15}$	**SS-PCVD**	**1.06**	**22.82**	**75.4**	**18.22**	**Our work**
$MAPbI_{3-x}Cl_x$	Vapor	1.07	21.5	67	15.4	[11]
$MAPbI_3$	Vapor	1.00	23.0	77	17.6	[32]
$CsPbI_3$	Vapor	1.06	13.8	71.6	10.5	[33]
$CsPbI_2Br$	Vapor	1.13	15.2	68	11.8	[34]
$CsPbBr_2I$	Vapor	0.96	8.7	56	4.7	[35]
$Cs_{.2}FA_{.8}PbI_{2.84}Br_{.16}$	Solution	1.07	21.9	74.2	17.35	[19]
$Cs_{.10}MA_{.90}PbI_3$	Solution	1.05	10.10	73	7.68	[28]
$FA_{.9}Cs_{.1}PbI_3$	Solution	1.06	23.5	66.3	16.5	[29]
$FA_{.9}Cs_{.1}PbI_3$	Solution	1.05	20.3	70	14.9	[36]
$Cs_{.05}(MA_{.17}FA_{.83})_{.95}Pb(I_{.83}Br_{.17})_3$	Solution	1.15	23.5	78.5	21.17	[37]

2. Experimental section

2.1. Device fabrication

The FTO substrates were rinsed by soap, acetone, ethanol and deionized water using ultrasonication, respectively. Then, FTO was coated with TiO_2 precursor (titanium isopropoxide) solution at a speed of 2000 rpm for 40 s. After sintering in the furnace at 500 °C for 30 min, the substrates were treated by $TiCl_4$ solution for 30 min at 70 °C and annealed at 500 °C for another 30 min to form the compact-TiO_2 layer. Then the CsBr and $PbBr_2$ film were deposited on the substrates by thermal evaporation in a vacuum system (~10^{-4} Pa), respectively. Then, the FTO/c-TiO_2/CsBr/$PbBr_2$ substrates and FAI powder were loaded in the furnace, followed by heating to 140 °C and kept for 100 min. After cooling down, the as-prepared perovskite film were rinsed by isopropanol (IPA) and annealed at 130 °C for 30 min. Subsequently, the hole transfer material (HTM) solution was deposited by spin-coating at a speed of 3500 rpm for 30 s, where 72.3 g Spiro-OMeTAD solution was dissolved in 1 mL chlorobenzene employed with addition of 17.5 µL Lithium bis(trifluoromethanesulfonyl) imide (Li-TFSI)/acetonitrile (520 mg/1 mL) and 28.8 µL tert-butylpyridine (tBP). Finally, 120 nm thickness of silver (Ag) electrode was deposited on the HTM by thermal evaporation with the active area of 0.09 cm^2. The $MAPbI_3$ hybrid perovskite film was deposited by the vapor deposition method in our previous work [12].

2.2. Characterization

The phase of products was identified by X-ray powder diffraction (XRD) utilizing a Cu Kα radiation with the scanning ranging from 10° to 70°. The morphology of the samples was investigated by the field emission scanning electron microscopy (FE-SEM, Sigma Zeiss/Hitachi-SU8020). Photocurrent density-voltage (J-V) measurements of perovskite solar cells were carried out on a Keithley 2636 system source meter with a Xenon Lamp Solar Simulator equipped with a light intensity of ~100 mW cm^{-2}. All the measurements were performed at the room temperature with the relative humidity of ~ 40%.

3. Results and discussion

As schematically illustrated in Fig. 1, the CsBr and $PbBr_2$ film were first deposited upon FTO/c-TiO_2 substrates by a physical vapor deposition process, and then loaded into a chemical vapor deposition system to deposit the perovskite film in the FAI atmosphere. After annealing in the air for 30 min, the HTM and Ag electrodes were coated above the perovskite absorption layer by spin-coating and thermal evaporation, respectively. More experimental details in the fabrication process are specified in the Experimental section. Fig. S1 in Supporting Information shows the photographs of the CsBr/$PbBr_2$ and the mixed-cation perovskite films. As we can see, the color of the perovskite thin films turns into yellow with the inclusion of more (or thicker) CsBr layer, which indicates that the $CsPbBr_3$ was formed. Meanwhile, the mixed-cation thin films deposited with the FAI addition appear constantly much darker (in black-brown color), indicating a much stronger light absorption over the full vision spectrum wavelengths.

Fig. 2 depicts the crystal structures of the pure FA-perovskite thin film, which has two distinct phases, that is, the non-perovskite δ phase in Fig. 2a with the trigonal lattice structure that exhibits a yellowish color and is known to be unfavorable for solar cell performance [19]; and the α phase with a hexagonal lattice structure showing a black color stabled after annealing above 160 °C, which is desirable for

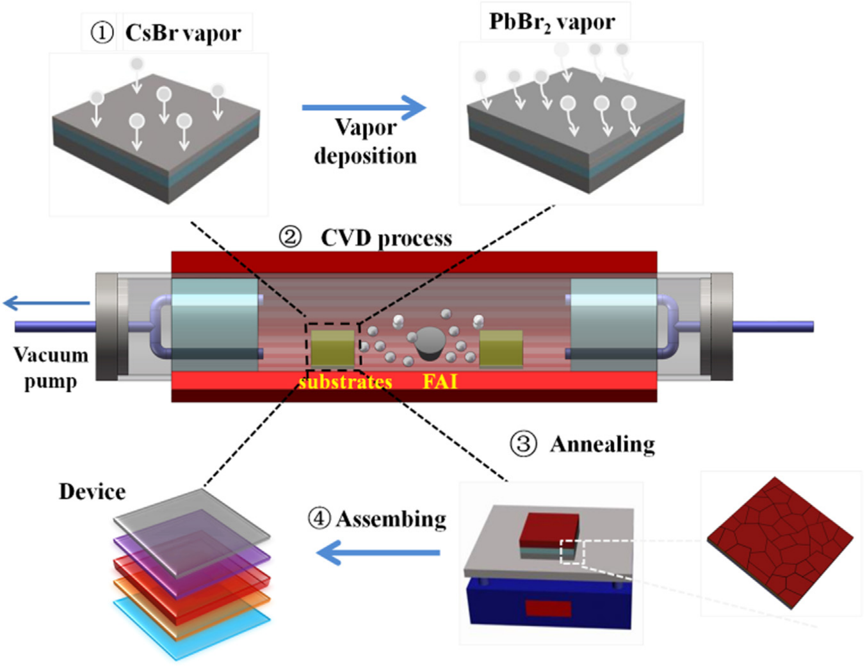

Fig. 1. The procedure of the perovskite film via a stack-sequence physical-chemical vapor deposition (SS-PCVD) method.

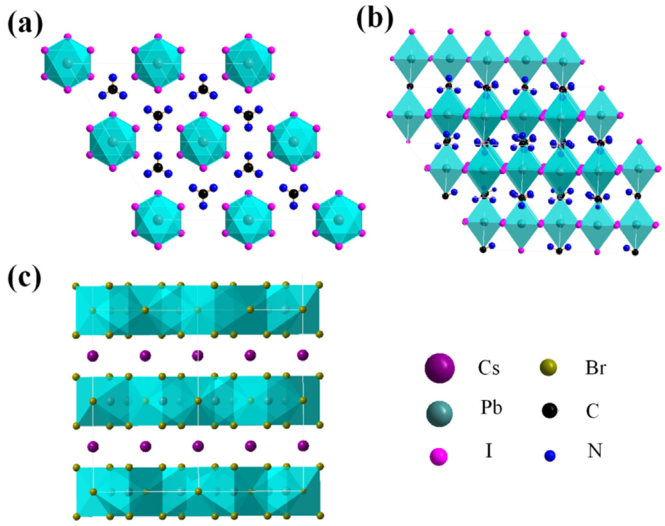

Fig. 2. (a) The trigonal structure (δ phase), (b) hexagonal (α phase) of the FA-perovskite and (c) the structure of $CsPb_2Br_5$ phase.

achieving a high performance perovskite photovoltaic. However, at the room temperature, a phase transition will easily happen that transforms the α-phase FA-perovskite into δ-phase, and thus leads to a decrease of the stability and the performance of the PSCs. Thus, the improvement of the stability of the FA-perovskite phase is crucial to achieve high performance PSCs. The X-ray diffraction of the perovskite films, as a function of the CsBr inclusion, was detected and presented in Fig. 3a-b and Fig. S2. The typical peak is detected at 14°, indicating that the perovskite film was formed after vapor deposition process. And the peak shifting towards higher angles, with more and more inclusion of CsBr layer, is indicative of a decrease in the lattice parameter [29]. Furthermore, the lattice parameters of perovskite without any CsBr is calculated to be a = b = 8.9811 Å, c = 10.9358 Å resulting in an unit cell volume of 763.91 $Å^3$, which is smaller to the pure $FAPbI_3$ unit cell reported in previous works, with the parameters of a = b = 8.9817 Å, c = 11.0060 Å and unit cell volume of 768.9 Å, respectively [40]. This change could be attributed to the incorporation of Br ionic with the radius of 1.96 Å, which is smaller than the I^- (2.2 Å). For the adding CsBr thickness of 10 nm, the corresponding lattice parameters of perovskite are calculated to be a = b = 8.9373 Å, c = 10.9054 Å and the cell volume of 754.36 Å, which is smaller than that of the pristine perovskite. This is due to the fact that the substituted Cs cations have a smaller ionic radius of 1.81 Å compared to that of FA^+ ($HC(NH_2)^{2+}$, 2.79 Å), and thus resulting in the reduction of cubo-octahedral volume for A-site cation surrounded by corner shared eight PbI_6 octahedral in unit cell [41]. Interestingly, the peaks at 11.66° and 29.35°, corresponding to the (002), (213) lattice planes, also emerge, which can be attributed to the formation of tetragonal $CsPb_2Br_5$ structures at the interface of the perovskite film. This indicates that as the content of the CsBr increasing, the $CsPb_2Br_5$ phase with a lattice structure as depicted in Fig. 2c is formed, following a reaction mechanism of $CsPbBr_3 + PbBr_2 \rightarrow CsPb_2Br_5$ [42], which is produced by $PbBr_8$ capped-triangular prisms in the a-b axis plane, leaving an expanded interlayer along the c-axis plane [43]. Moreover, the absorption and photoluminescence (PL) spectra of the perovskite films were also measured and presented in Fig. 3c and Fig. S3 in Supporting Information, showing in general a blue-shifting of PL peak (~10 nm in Fig. S3) and a much stronger absorption (Fig. 3c) with the increment of the adding CsBr layer thickness. According to the Kubelka-Munk equation and plots in Fig. 3d, the band gaps of the perovskite thin films are extracted and found to increase from 1.52 eV to 1.62 eV with a thicker CsBr layer. These observations imply that the optical band gap of the mixed-cation perovskite thin films can be well controlled by tuning the CsBr layer thickness, which can also be assigned to the reduced lattice parameters with the slightly-enhanced binding energy of the Pb-I.

In order to investigate the influence of Cs and Br incorporation, the X-ray photoelectron spectroscopy was also carried out as the shrinkage of the cubo-octahedral volume could lead to a change of the chemical bonding nature between Pb and I. As witnessed in Fig. S4a, there is no Cs 3d peak detected in the pristine perovskite films, while the corresponding Cs peaks appear only with the introduction of CsBr layers, indicating that the Cs cations are forming bonds with the halide element. The shifting of the two dominant peaks at 137.9 eV and 142.8 eV in Fig. S4b, corresponding to those of Pb4 f7/2 and 4 f 5/2 levels, towards higher binding energies, accompanied with the same trend of I 3d peaks in Fig. S4c also to higher binding energy, suggests that the

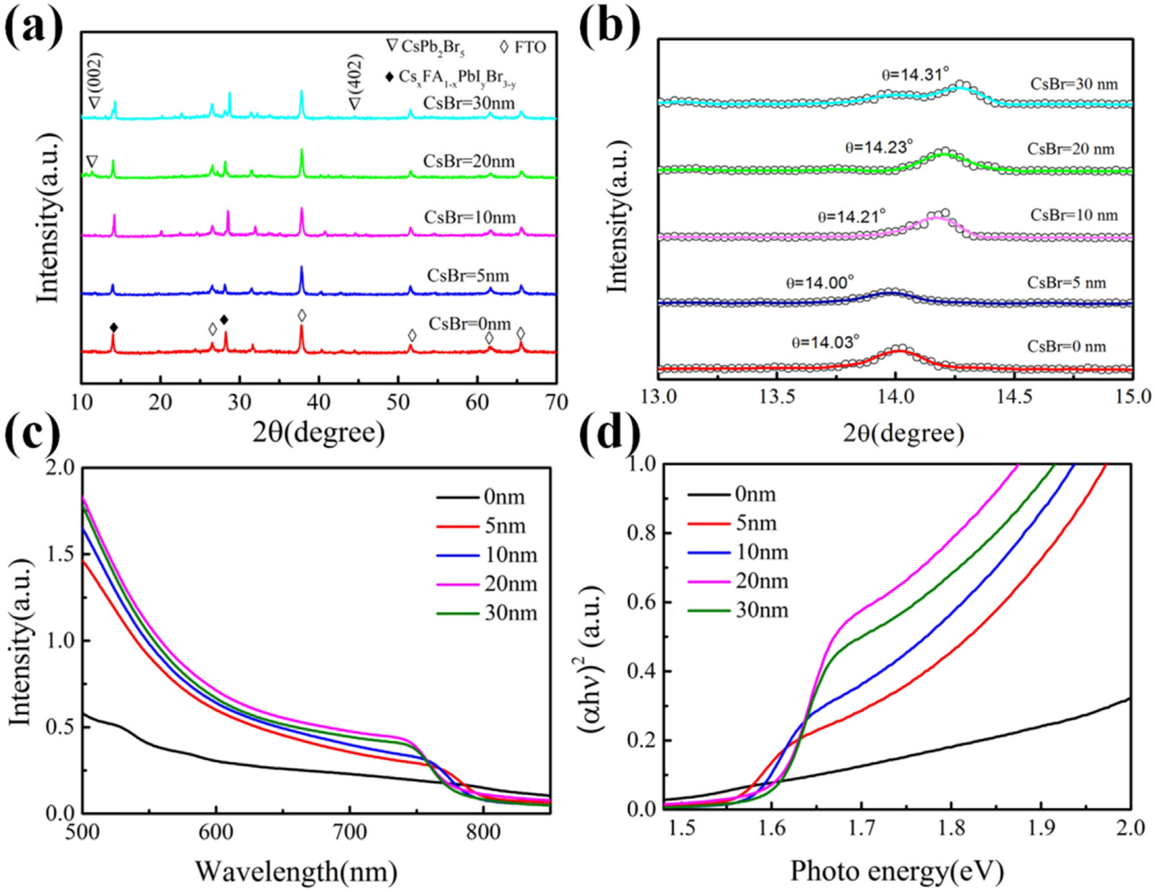

Fig. 3. (a) shows the X-ray diffraction patterns, with a magnified view of the (101) peak corresponding to the mixed-perovskite films shown in (b); (c) and (d) present the absorption spectra and the transformed Kubelka–Munk spectra of the perovskite films with various thicknesses of adding CsBr layers, respectively.

lattice parameter is slightly decreased with the Cs doping [19,36]. Following the Br introducing, the intensity of the Br 3d peak in Fig. S4d also increases, suggesting that the Br atoms are incorporated gradually into the perovskite lattice structure with a thicker CsBr layer. The ratio of Cs/Pb and Br/Pb are estimated to be 0.13:1 and 0.14:1 for the CsBr thickness of ~10 nm. Based on these estimations, the mixed-perovskite thin film prepared in this work has an overall formula of $Cs_{.15}FA_{.85}PbI_{2.85}Br_{.15}$ [35,36]. Notably, as mentioned above, the $CsPb_2Br_5$ is formed at the interface or boundary of the perovskite thin film, which could increase the concentration of Br.

The morphology of the perovskite films produced with various CsBr thicknesses is examined by SEM and shown in Fig. 4 and Fig. S5. The pristine perovskite film without any Cs inclusion exhibits a poor coverage, with large pine-holes/voids due to the decomposition of $FAPbI_xBr_{3-x}$ perovskite. In fact, the black pure $FAPbI_3$ perovskite phase is stable only at 160 °C, and prone to transfer into yellowish (δ) phase below this phase transition temperature. So, a fast decomposition occurred shortly after their deposition and exposure to air at room temperature. Thus, plenty of voids are left after post-annealing in the air with the FAI vitalization. Remarkably, there is no such phase change observed for the perovskite thin film with the introduction of Br into the $FAPbI_3$ film to form the $FAPbI_xBr_{3-x}$. Following the incorporation of CsBr film, the perovskite film becomes more denser with larger crystals and clear grain boundaries, indicating that the introduction of Cs cations is favorable for the formation of perovskite phase, and for improving the crystallization of the perovskite thin films. The element distribution mapping of the perovskite film, presented in Fig. S6, verified that the Cs atoms have been homogeneously distributed into the perovskite absorption layer via the vapor formation process. A typical cross-section SEM image of the PSCs is shown in Fig. 4g, revealing a full coverage of dense perovskite film with a thickness of ~400 nm.

As mentioned above, an ultra-thin $CsPb_2Br_5$ film was formed between the TiO_2 and the $PbBr_2$ film, which is known to be a wide band gap materials of ~2.9 eV [43]. As depicted in Fig. 5a, the oxygen vacancies at the interface of the TiO_2 film usually serve as deep electron-donating sites for the recombination of the photo-carriers, and also, the photocatalytic effect in TiO_2 can accelerate the decomposition of perovskite under ultraviolet illumination. To address these problems, the $CsPb_2Br_5$ affords abundant halogen, which is accumulated at the interface and connected with the cations, and thus can help to prevent the trapping of excited electrons by the surface defects and reduce the recombination of the photo-carrier [44,45]. In addition, it is also suggested that the reduced carrier recombination with the presence of $CsPb_2Br_5$ in the perovskite film is related to the favorable energy band alignment, which is similar to that of PbX_2 and $BaSnO_3$ [46–48]. In the following, the perovskite photovoltaics are assembled in a typical structure of FTO/c-TiO_2/perovskite/Spiro-OMeTAD/Ag, where perovskite film is defined as $Cs_xFA_{1-x}PbI_yBr_{3-y}$. The FAI vapor diffused into the precursor layer, as schematically depicted in the Fig. 5b, to form a gradient absorption layer along the vertical direction. The bottom layer (with a higher content of the Cs and Br) thus exhibits a wider band gap, while the top layer (with a higher content of FAI vapor, as it is diffused and introduced from the top surface) has a narrower band gap. Meanwhile, it is noted that the open circuit voltage of the PSCs are determined by the band gap of the absorption layer, particularly the highest occupied molecular orbital (HOMO) of the electron donor (the mixed-cation perovskite) and the lowest unoccupied molecular orbital (LUMO) of the electron acceptor (TiO_2) [49]. Fig. 5c presents the energy diagram of the mixed-cation perovskite devices, where the perovskite film with excess Cs and Br provides a lower HOMO that could

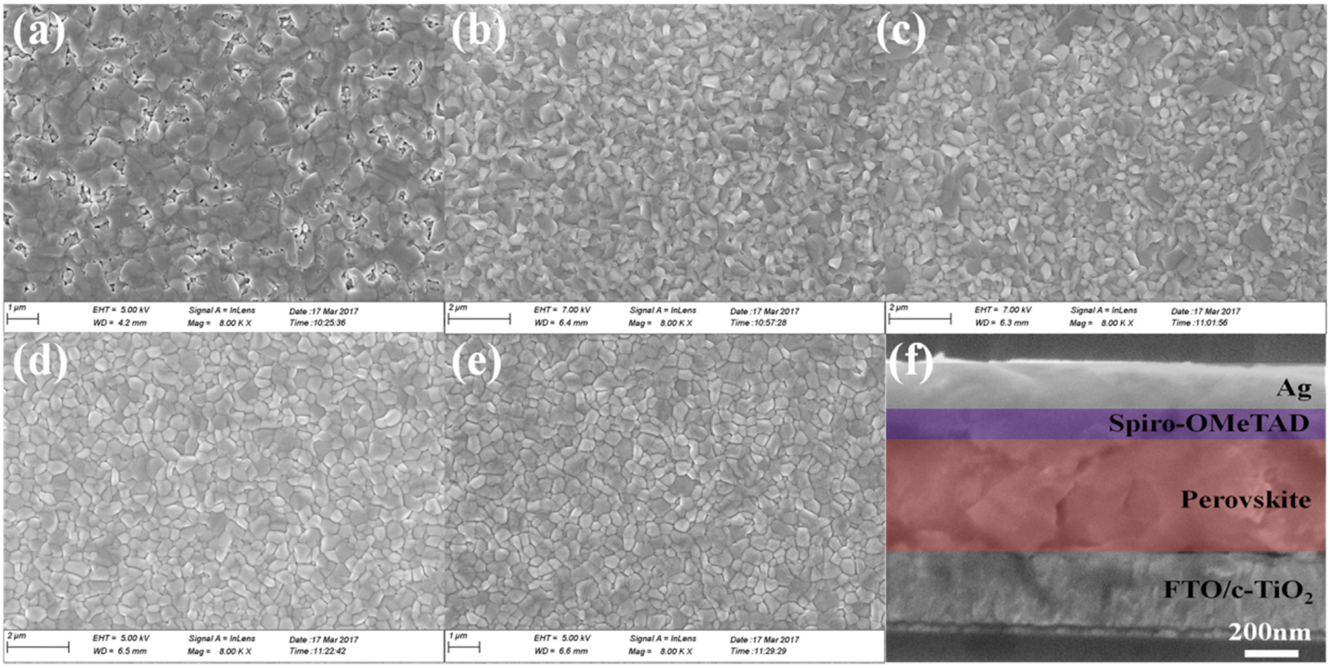

Fig. 4. The SEM images of the perovskite films, produced a CsBr thickness of (a) 0 nm, b) 5 nm, (c) 10 nm, (d) 20 nm, (e) 30 nm. (f) shows the typical cross-section SEM image of the PSCs.

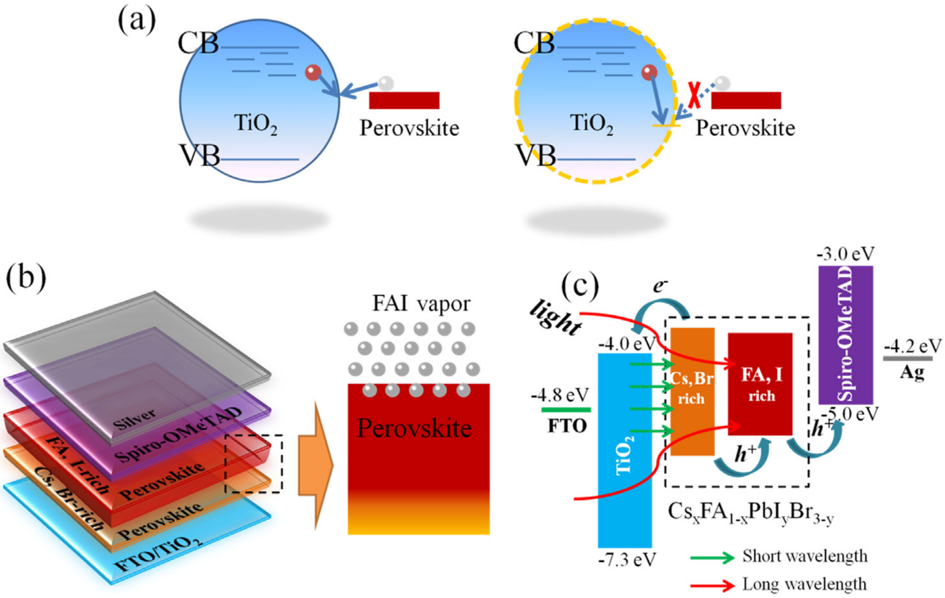

Fig. 5. (a) Illustrates interface passivation by the formation of $CsPb_2Br_5$ ultra-thin film. (b) The schematic diagram of the vapor doping process. (c) Energy diagram of the PSCs via the SS-PCVD process.

help to increase the voltage output of PSCs.

In addition, it is also important to point out that, as the incident light will be shed in from left, through the TiO_2/FTO, the wider band gap (Cs, Br rich) perovskite layer will absorb only the high energy photons, while leaving the low energy ones into the inner narrow band gap layer to get absorbed there. This distributed light absorption is beneficial as it leads to a more uniform distribution of the photo-carrier generation throughout the perovskite thin film, and thus shortens the transport distance for holes to be collected at the inner HTL layer, as illustrated in Fig. 5c, the transport of holes could gain further acceleration towards the inner HTL layer, as the gradient band gap variation (wider in outer layer and narrower in inner layer) can establish an effective built-in field that drives the photo-generated holes towards inner HTL layer. This gradient band gap profile is also beneficial to photo-carrier separation and collection, but normally does not exist within uniform ingredient and band gap materials. Additionally, the ultra smooth and good contacting of the perovskite devices produced by vapor deposition can effectively reduce the contact resistance. The electrochemical impedance spectroscopy (EIS) was conducted under a reverse potential of 1.0 V in the dark condition. The Nyquist plots in Fig. S7 presents a smaller R_{co} value of 600.78 $\Omega\,cm^2$ for vapor-processed than the solution-processed (2237 $\Omega\,cm^2$), suggesting that the film produced by vapor method with dense and large crystals facilitate the electron/hole transport at the interface.

Finally, the current-voltage (J-V) curves of the mix-cation PSCs, with different CsBr layer thicknesses, were characterized under

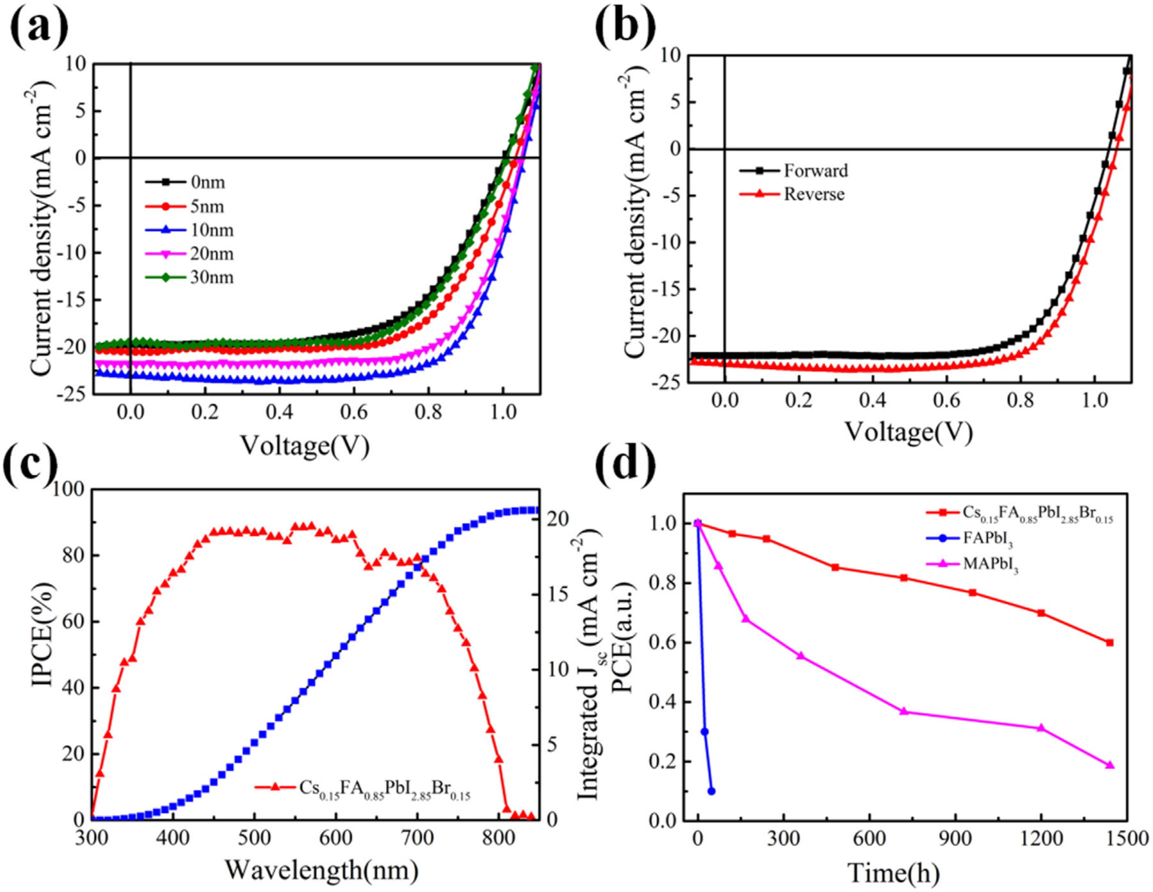

Fig. 6. (a) The J-V curve of the PSCs with various thickness of CsBr. (b) The J-V curve of the PSC under forward and reverse scan. (c) The IPCE spectrum of the champion device. (d) Comparison of the stability of $FAPbI_3$, $MAPbI_3$ and $Cs_{.15}FA_{.85}PbI_{2.85}Br_{.15}$ perovskite devices.

Table 2
The parameters of the pure FA, MA and mixed cation PSCs.

Composition	V_{oc} (V)	J_{sc} (mA cm^{-2})	FF (%)	PCE (%)
$FAPbI_3$	0.96	19.93	61.1	11.69
$MAPbI_3$	1.03	21.25	69.0	15.10
$Cs_{.15}FA_{.85}PbI_{2.85}Br_{.15}$	1.06	22.82	75.4	18.22

standard AM 1.5 illumination and shown in Fig. 6a, while corresponding parameters are summarized in the Table S1. The pure $FAPbI_{3-y}Br_y$ gives a lower power conversion of 12.48%, with V_{oc}, J_{sc} and FF of 0.99 V, 19.82 mA cm^{-2} and 63%, respectively, which is higher than that of pure $FAPbI_3$ device with a PCE of 11.69% (Table 2). This can be ascribed to the bromine incorporation into the perovskite to replace the iodine, thus increasing the band gap of the perovskite film leading to a higher voltage output. Following the inclusion of 10 nm CsBr layers, the mixed hybrid PSCs achieved a higher PCE of 14.01%. Then, at the CsBr layer thickness of 10 nm, the PSC devices exhibited the highest PCE of 18.22%, with a V_{oc} of 1.06 V, J_{sc} of 22.82 mA cm^{-2} and FF of 75.4%. However, further increasing of the CsBr layer leads to only a significant decrease of PCE to 13.14%, mainly as a result of the dropping of J_{sc} and FF. This could be limited by the fact that the present of a thicker and thicker $CsPb_2Br_5$ layer at the interface of TiO_2/perovskite will eventually block the electrons transport, and thus leading to a lower photocurrent and higher series resistance. Thus, the amount of the $CsPb_2Br_5$ should be better controlled to trade-off the contributions of interface passivation and carrier transport or collection at the TiO_2/perovskite interface [44,45]. Fig. S8 shows the PCE histograms of the pure or mixed cation devices, which emphasize the superior performance of the vapor-processed mixed cation perovskite solar cells with a higher PCE distribution ranging from 14%~19%.

More importantly, we found that the improvement of the fill factor from 72% to 75.4%, accompanied with the photocurrent density increase from 22.17 mA cm^{-2} to 22.82 mA cm^{-2} (Table S2) were detected from the Fig. 6b, suggesting that a little hysteresis phenomenon is observed in the mixed-cation PSC devices, which is attributed to the planar structure of the perovskite devices. The incident-photon-to-current conversion efficiency (IPCE) spectrum of the PSC device with $Cs_{.15}FA_{.85}PbI_{2.85}Br_{.15}$, is presented in Fig. 6c, which is also compared to the pure $FAPbI_3$ and $MAPbI_3$ are shown in Fig. 6c and Fig. S9. The integrated current density of the devices for $Cs_{.15}FA_{.85}PbI_{2.85}Br_{.15}$, pure $FAPbI_3$ and $MAPbI_3$ are 20.7 mA cm^{-2}, 18.3 mA cm^{-2} and 20.1 mA cm^{-2}, respectively, which is in agreement with the J_{sc} derived from the J-V curves (seen in Fig. S10).

Since the stability is an important parameter for the PSCs, we focus on the performance of the device in the moisture environment. As seen in Fig. S11, the color of pristine perovskite film turned to white after stored in the air with the humidity of ~40% for one month, which indicates the decomposition of the perovskite. However, no change of the perovskite film with the CsBr incorporation and the dark color indicate that there is no decomposition. Even after stored for the two months without any encapsulation, the perovskite film still shows a dark color, suggesting a little decomposition is observed. Fig. S12 and Table S3 are the J-V curves of the mixed-PSCs after stored in the air for more than two months. The mixed PSCs is much stable than pure $FAPbI_3$ and $MAPbI_3$ based PSCs under ambient environment without particular encapsulation. The compacted and uniformed perovskite absorption layer can be clearly seen in the cross-section SEM image (Fig. S13) after stored in the air for more than two months, indicating that the devices exhibit a high stability and keep the integrity of the device structure. Meanwhile, incorporating the inorganic material into the perovskite film through the vapor-solid reaction via the SS-PCVD can effectively avoid the solvent damage and metastable state during the reaction process. As a consequence, the mixed cation PSCs suffer only a little degradation within 480 h, and the PCE of device is still more than 10% even after 1400 h later exposure. On the contrary, the performance of pure $FAPbI_3$ decreased within 48 h at the same condition, and the pure $MAPbI_3$ also dropped significantly after 72 h later, as seen in Fig. S14, and only 2.4% PCE was obtained after stored in the air for two months later.

4. Conclusions

In conclusion, a vapor doping perovskite film, for the first time, was employed with the CsBr as the precursor material. The perovskite film derived this method exhibited a full coverage absorption layer with the grain size of 500 nm. Intriguingly, a high performance increasing was realized by incorporated CsBr into the pure $FAPbI_3$ structure with the thickness of 10 nm, 45% enhancement was obtained in the devices. The SS-PCVD presents a simple, well control, and low cost approach to obtain a high quality perovskite film and photovoltaics. More importantly, the mixed PSCs show a high stability, enabling suffers from a high wet condition comparing to the pure $FAPbI_3$ and $MAPbI_3$. Our method to fabricate the mixed cation perovskite film based on the vapor doping process provides a new approach.

Acknowledgements

This work was financed by Scientific and Technological Support Program in Jiangsu province under No. BE2014147-2, NSFC under No. 61674075, 11274155, 61204050, U1632151, Open Research Fund of State Key Laboratory of Pulsed Power Laser Technology of China (Hefei, SKL 2015 KF 04), JSNSFC No. BK20150275, Jiangsu Shuangchuang Team's and Personal Program, Jiangsu Excellent Young Scholar Program and the Fundamental Research Funds for the Central Universities.

Appendix A. Supplementary material

Supplementary data associated with this article can be found in the online version at http://dx.doi.org/10.1016/j.nanoen.2018.04.012.

References

[1] Q. Tai, F. Yan, Adv. Mater. 29 (2017) 1700192–1700228.
[2] National Renewable Energy Laboratory, Best Research Cell Efficiency, ⟨http://www.nrel.gov/ncpv/images/efficiency_chart.jpg⟩ (accessed January 2016).
[3] A. Kojima, K. Teshima, Y. Shirai, T. Miyasaka, J. Am. Chem. Soc. 131 (2009) 6050–6051.
[4] Y. Lin, B. Chen, F. Zhao, X. Zheng, Y. Deng, Y. Shao, Y. Fang, Y. Bai, C. Wang, J. Huang, Adv. Mater. 29 (2017) 1700607–1700614.
[5] X. Liu, T. Bu, J. Li, J. He, T. Li, J. Zhang, W. Li, Z. Ku, Y. Peng, F. Huang, Y.-B. Cheng, J. Zhong, Nano Energy 44 (2018) 34–42.
[6] M. Li, Z.-K. Wang, T. Kang, Y. Yang, X. Gao, C.-S. Hsu, Y. Li, L.-S. Liao, Nano Energy 43 (2018) 47–54.
[7] F. Ye, H. Chen, F. Xie, W. Tang, M. Yin, J. He, E. Bi, Y. Wang, X. Yang, L. Han, Energy Environ. Sci. 9 (2016) 2295–2301.
[8] N.J. Jeon, J.H. Noh, Y.C. Kim, W.S. Yang, S. Ryu, S.I. Seok, Nat. Mater. 13 (2014) 897–903.
[9] Q. Chen, H. Zhou, Z. Hong, S. Luo, H.S. Duan, H.H. Wang, Y. Liu, G. Li, Y. Yang, J. Am. Chem. Soc. 136 (2014) 622–625.
[10] M.R. Leyden, L.K. Ono, S.R. Raga, Y. Kato, S. Wang, Y. Qi, J. Mater. Chem. A 2 (2014) 18742–18745.
[11] M. Liu, M.B. Johnston, H.J. Snaith, Nature 501 (2013) 395–398.
[12] G. Tong, Z. Song, C. Li, Y. Zhao, L. Yu, J. Xu, Y. Jiang, Y. Sheng, Y. Shi, K. Chen, RSC Adv. 7 (2017) 19457–19463.
[13] G.E. Eperon, V.M. Burlakov, P. Docampo, A. Goriely, H.J. Snaith, Adv. Funct. Mater. 24 (2014) 151–157.
[14] C. Liu, K. Wang, C. Yi, X. Shi, A.W. Smith, X. Gong, A.J. Heeger, Adv. Funct. Mater. 26 (2016) 101–110.
[15] T.M. Koh, K. Fu, Y. Fang, S. Chen, T.C. Sum, N. Mathews, S.G. Mhaisalkar, P.P. Boix, T. Baikie, J. Phys. Chem. C 118 (2014) 16458–16462.
[16] G.E. Eperon, S.D. Stranks, C. Menelaou, M.B. Johnston, L.M. Herz, H.J. Snaith, Energy Environ. Sci. 7 (2014) 982–988.
[17] S. Pang, H. Hu, J. Zhang, S. Lv, Y. Yu, F. Wei, T. Qin, H. Xu, Z. Liu, G. Cui, Chem. Mater. 26 (2014) 1485–1491.
[18] J.W. Lee, D.J. Seol, A.N. Cho, N.G. Park, Adv. Mater. 26 (2014) 4991–4998.
[19] C. Yi, J. Luo, S. Meloni, A. Boziki, N. Ashari-Astani, C. Grätzel, S.M. Zakeeruddin, U. Röthlisberger, M. Grätzel, Energy Environ. Sci. 9 (2016) 656–662.
[20] J. Liang, C. Wang, Y. Wang, Z. Xu, Z. Lu, Y. Ma, H. Zhu, Y. Hu, C. Xiao, X. Yi, G. Zhu, H. Lv, L. Ma, T. Chen, Z. Tie, Z. Jin, J. Liu, J. Am. Chem. Soc. 138 (2016) 15829–15832.
[21] J. Song, L. Xu, J. Li, J. Xue, Y. Dong, X. Li, H. Zeng, Adv. Mater. 28 (2016) 4861–4869.
[22] A. Swarnkar, A.R. Marshall, E.M. Sanehira, B.D. Chernomordik, D.T. Moore, J.A. Christians, T. Chakrabarti, Jeffrey A. Christians, Tamoghna Chakrabarti, Joseph M. Luther, Science 354 (2016) 92–95.
[23] X. Li, Y. Wu, S. Zhang, B. Cai, Y. Gu, J. Song, H. Zeng, Adv. Funct. Mater. 26 (2016) 2435–2445.
[24] R.G. Niemann, L. Gouda, J. Hu, S. Tirosh, R. Gottesman, P.J. Cameron, A. Zaban, J. Mater. Chem. A 4 (2016) 17819–17827.
[25] M. Deepa, M. Salado, L. Calio, S. Kazim, S.M. Shivaprasad, S. Ahmad, Phys. Chem. Chem. Phys. 19 (2017) 4069–4077.
[26] G. Tong, X. Lan, Z. Song, G. Li, H. Li, L. Yu, J. Xu, Y. Jiang, Y. Sheng, Y. Shi, K. Chen, Mater. Today Energy 5 (2017) 173–180.
[27] Y. Jiang, M.R. Leyden, L. Qiu, S. Wang, L.K. Ono, Z. Wu, E.J. Juarez-Perez, Y. Qi, Adv. Funct. Mater. 28 (2018) 1703835–1703847.
[28] H. Choi, J. Jeong, H.-B. Kim, S. Kim, B. Walker, G.-H. Kim, J.Y. Kim, Nano Energy 7 (2014) 80–85.
[29] J.-W. Lee, D.-H. Kim, H.-S. Kim, S.-W. Seo, S.M. Cho, N.-G. Park, Adv. Energy Mater. 5 (2015) 1501310–1501318.
[30] Y.H. Park, I. Jeong, S. Bae, H.J. Son, P. Lee, J. Lee, C.-H. Lee, M.J. Ko, Adv. Funct. Mater. 27 (2017) 1605988–1605996.
[31] M. Saliba, T. Matsui, K. Domanski, J.Y. Seo, A. Ummadisingu, S.M. Zakeeruddin, J.P. Correabaena, W.R. Tress, A. Abate, A. Hagfeldt, M. Grätzel, Science 354 (2016) 206–209.
[32] A. Ng, Z. Ren, Q. Shen, S.H. Cheung, H.C. Gokkaya, S.K. So, A.B. Djurisic, Y. Wan, X. Wu, C. Surya, ACS Appl. Mater. Interfaces 8 (2016) 32805–32814.
[33] L.A. Frolova, D.V. Anokhin, A.A. Piryazev, S.Y. Luchkin, N.N. Dremova, K.J. Stevenson, P.A. Troshin, J. Phys. Chem. Lett. 8 (2017) 67–72.
[34] C.Y. Chen, H.Y. Lin, K.M. Chiang, W.L. Tsai, Y.C. Huang, C.S. Tsao, H.W. Lin, Adv. Mater. 29 (2017) 1605290–1605296.
[35] Q. Ma, S. Huang, X. Wen, M.A. Green, A.W.Y. Ho-Baillie, Adv. Energy Mater. 6 (2016) 1502202–1502206.
[36] X. Xia, W. Wu, H. Li, B. Zheng, Y. Xue, J. Xu, D. Zhang, C. Gao, X. Liu, RSC Adv. 6 (2016) 14792–14798.
[37] M. Saliba, T. Matsui, J.Y. Seo, K. Domanski, J.P. Correa-Baena, M.K. Nazeeruddin, S.M. Zakeeruddin, W. Tress, A. Abate, A. Hagfeldt, M. Gratzel, Energy Environ. Sci. 9 (2016) 1989–1997.
[38] X. Li, D. Bi, C. Yi, J.-D. Décoppet, J. Luo, S.M. Zakeeruddin, A. Hagfeldt, M. Grätzel, Science 353 (2016) 58–62.
[39] G. Tong, X. Geng, Y. Yu, L. Yu, J. Xu, Y. Jiang, Y. Sheng, Y. Shi, K. Chen, RSC Adv. 7 (2017) 18224–18230.
[40] C.C. Stoumpos, C.D. Malliakas, M.G. Kanatzidis, Inorg. Chem. 52 (2013) 9019–9038.
[41] A. Amat, E. Mosconi, E. Ronca, C. Quarti, P. Umari, M.K. Nazeeruddin, M. Gratzel, F. De Angelis, Nano Lett. 14 (2014) 3608–3616.
[42] K.H. Wang, L. Wu, L. Li, H.B. Yao, H.S. Qian, S.H. Yu, Angew. Chem. Int. Ed. 55 (2016) 8328–8332.
[43] G. Li, H. Wang, Z. Zhu, Y. Chang, T. Zhang, Z. Song, Y. Jiang, Chem. Commun. 52 (2016) 11296–11299.
[44] X. Zhang, B. Xu, J. Zhang, Y. Gao, Y. Zheng, K. Wang, X.W. Sun, Adv. Funct. Mater. 26 (2016) 4595–4600.
[45] G. Tong, H. Li, D. Li, Z. Zhu, E. Xu, G. Li, L. Yu, J. Xu, Y. Jiang, Small 14 (2018) 1702523–1702530.
[46] Q. Chen, H. Zhou, T.B. Song, S. Luo, Z. Hong, H.S. Duan, L. Dou, Y. Liu, Y. Yang, Nano Lett. 14 (2014) 4158–4163.
[47] S.S. Shin, E.J. Yeom, W.S. Yang, S. Hur, M.G. Kim, J. Im, J. Seo, J.H. Noh, S.I. Seok, Science 356 (2017) 167–171.
[48] Y.C. Kim, N.J. Jeon, J.H. Noh, W.S. Yang, J. Seo, J.S. Yun, A. Ho-Baillie, S. Huang, M.A. Green, J. Seidel, T.K. Ahn, S.I. Seok, Adv. Energy Mater. 6 (2016) 1502104–1502111.
[49] J. Chang, H. Zhu, J. Xiao, F.H. Isikgor, Z. Lin, Y. Hao, K. Zeng, Q.-H. Xu, J. Ouyang, J. Mater. Chem. A 4 (2016) 7943–7949.